3–D Surface Topography Boundary Conditions in Seismic Wave Modelling

Stig Hestholm
Earth Resources Laboratory, Massachusetts Institute of Technology,
42 Carleton Street, Cambridge, MA 02142, USA

Bent Ruud
University of Bergen, Dept. of Solid Earth Physics,
Allégt. 41, N–5007 Bergen, Norway

Abstract

New alternative formulations of exact boundary conditions for arbitrary three–dimensional (3–D) free surface topographies on seismic media have been derived. They are shown to be equivalent with previously published formulations, thereby serving as a verification of the validity of each set of formulations. The top of a curved grid represents the free surface topography while the grid's interior represents the physical medium. We assume the velocity–stress version of the viscoelastic wave equations to be valid in this grid before transforming the equations to a rectangular grid. In order to do the numerical discretization we apply the latter version of equations for seismic wave propagation simulation in the interior of the medium. The numerical discretization of the free surface topography boundary conditions by second–order finite–differences (F–Ds) is shown in detail, as well as spatially unconditional stability of the resulting system of equations. The F–D order is increased by two for each point away from the free surface up to eight, which is the order used in the interior. We use staggered grids both in space and time and the second–order leap–frog and Crank–Nicholson methods for wavefield time propagation.

We simulate point sources at the surface of a homogeneous medium, with a plane surface containing a hill and a trench, respectively. The main features of these general cases are outlined. Then, we present results using parameters typical of teleseismic earthquakes and explosions with a 200×100 km^2 area of real topography from southwestern Norway over a homogeneous medium. A dipping plane wave simulates a teleseismic P–wave incident on the surface topography. Results show clear conversion from P– to Rg–(short period fundamental mode Rayleigh) waves in the steepest and/or roughest topography, as well as attenuated waves in valleys and fjords. The codes are parallellized for simulation on fast supercomputers to model higher frequencies and/or larger areas than before.

1 Introduction

The free surface involves the strongest discontinuity we encounter in seismic wave modelling. Inclusion of topography along such a surface is therefore important, and even more so the stronger gradients and/or irregularities the local topography exhibits (Hestholm and Ruud, 1998). Topographic data also has the smallest error margins of any medium parameters, and thus should be used in modelling when available. The method used in this paper combines curved grid wave equations with explicit expressions for the particle velocities at the surface topography. No extra memory is needed (except for the topography data) and only marginal extra simulation cost is required compared to the modelling of a free plane surface.

The literature on 3–D free surface topography modelling is limited. The 2–D work of Jih et al. (1988) and Robertsson (1996) categorize types of surface points for separate treatment. Ohminato and Chouet (1997) use a 3–D analogous procedure modelling surface topography in a 'stair–case' manner. Komatitsch et al. (1996) apply a tensorial formulation of the wave equations for modelling curved interfaces and free surface topography, which is accurate but requires a lot of memory. The boundary element method (Sanchez-Sesma and Campillo, 1991) has been used

mainly to model relatively simple geometric features because the discretization applied to each structure must be given specifically to avoid instabilities. citetBouchon96 devised a space–frequency domain version of the method.

Tessmer and Kosloff (1994) and Tessmer et al. (1992) transformed the velocity–stress formulation of the elastic wave equations from a curved to a rectangular grid. This procedure was subsequently used by Hestholm and Ruud (1994) among others. An immediate advantage of using the velocity–stress formulation is that we do not differentiate material parameters across discontinuities (Virieux, 1986). Tessmer and Kosloff (1994) applied an iterative treatment to stresses and particle velocities at the surface topography, whereas here we derive explicit, exact conditions for the particle velocities at the free surface assuming a curved grid is adapted to this surface. Our method transforms both the internal medium equations as well as the free surface boundary conditions from the curved to a rectangular grid where the numerical computations can be performed. Seismic wave modelling using curved grids was originally used to adapt grids to interior interfaces (Fornberg, 1988b).

In this paper, we derive new formulations of boundary conditions for free surface topography by substituting versions of the medium equations valid for a curved grid in the limit of a free surface, directly into the vanishing normal stress condition generally valid at free surfaces. The resulting set of equations is shown to be equivalent with the one derived by Hestholm (1999), and hence serves as a verification of its validity. Both sets of equations are exact closed systems for the particle velocities at a free surface. We note that the use of imaging points above the free surface (Levander, 1988) is not an alternative because the symmetry conditions assumed by such methods are broken with the introduction of a curved grid. Also, from our experience, the use of non–centred F–D operators (Fornberg, 1988a) for discretization of the boundary conditions leads to instabilities in time.

We give the first–order system of viscoelastic equations of motion for a curved grid (Hestholm, 1999) based on the Cartesian velocity–stress formulation (Robertsson et al., 1994) originally developed for the displacement–stress version (Carcione et al., 1988). Then, we derive new formulations of boundary conditions for free surface topography. We also give a description of the numerical solution and show unconditional stability in space of the system resulting from discretization of the boundary conditions. Next, we show simulations of a hill and a depression, respectively, located on an otherwise plane surface of a homogeneous medium. Lastly, we show a viscoelastic scattering simulation of a dipping incident plane wavefront of teleseismic P–waves in a homogeneous medium containing a large area of fjord–topography from southwestern Norway.

2 Viscoelastic Wave Modelling Formulation

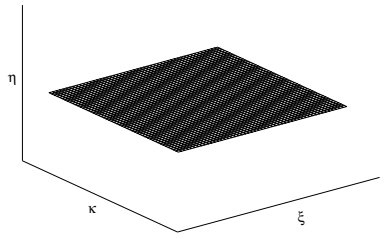

Figure 1: Rectangular grid surface.

We introduce a linear mapping from a rectangular (ξ, κ, η)–grid (Figure 1) to a curved grid in the (x, y, z)–system (Figure 2), where both grids have positive direction upwards. The 3–D mapping can be written

$$x(\xi, \kappa, \eta) = \xi, \tag{1}$$

$$y(\xi, \kappa, \eta) = \kappa, \tag{2}$$

$$z(\xi, \kappa, \eta) = \frac{\eta}{\eta_{max}} z_0(\xi, \kappa), \tag{3}$$

where $z_0(\xi, \kappa)$ is the topography function, and the rectangular (ξ, κ, η)–grid is bounded by $\xi = 0$, $\xi = \xi_{max}$ and $\kappa = 0$, $\kappa = \kappa_{max}$ horizontally and $\eta = 0$ and $\eta = \eta_{max}$ vertically. The degree of stretching of the curved grid in the

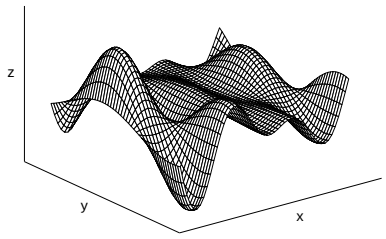

Figure 2: Curved grid surface.

(x, y, z)–system is proportional to the height above the bottom plane ($z = 0$). We assume the curved grid (Figure 2) to be located in a Cartesian (x, y, z) coordinate system where the velocity–stress formulation of the viscoelastic wave equations are valid. Then, we transform the equations into the rectangular, computational (ξ, κ, η)–grid (Figure 1) by using the chain rule for the variables and employing expressions for the partial derivatives of the coordinates (Hestholm, 1999),

$$\frac{\partial \xi}{\partial x} = 1, \qquad \frac{\partial \xi}{\partial y} = 0, \qquad \frac{\partial \xi}{\partial z} = 0, \tag{4}$$

$$\frac{\partial \kappa}{\partial x} = 0, \qquad \frac{\partial \kappa}{\partial y} = 1, \qquad \frac{\partial \kappa}{\partial z} = 0, \tag{5}$$

$$A(\xi,\kappa,\eta) \equiv \frac{\partial \eta}{\partial x} = -\frac{\eta}{z_0(\xi,\kappa)} \frac{\partial z_0(\xi,\kappa)}{\partial \xi}, \tag{6}$$

$$B(\xi,\kappa,\eta) \equiv \frac{\partial \eta}{\partial y} = -\frac{\eta}{z_0(\xi,\kappa)} \frac{\partial z_0(\xi,\kappa)}{\partial \kappa}, \tag{7}$$

$$C(\xi,\kappa) \equiv \frac{\partial \eta}{\partial z} = \frac{\eta_{max}}{z_0(\xi,\kappa)}. \tag{8}$$

We obtain the velocity–stress formulation of the viscoelastic medium equations with one relaxation mechanism in the rectangular (ξ, κ, η)–grid (Hestholm, 1999),

$$\rho \frac{\partial u}{\partial t} = \frac{\partial \sigma_{xx}}{\partial \xi} + A(\xi,\kappa,\eta)\frac{\partial \sigma_{xx}}{\partial \eta} + \frac{\partial \sigma_{xy}}{\partial \kappa} + B(\xi,\kappa,\eta)\frac{\partial \sigma_{xy}}{\partial \eta} + C(\xi,\kappa)\frac{\partial \sigma_{xz}}{\partial \eta} + f_x, \tag{9}$$

$$\rho \frac{\partial v}{\partial t} = \frac{\partial \sigma_{xy}}{\partial \xi} + A(\xi,\kappa,\eta)\frac{\partial \sigma_{xy}}{\partial \eta} + \frac{\partial \sigma_{yy}}{\partial \kappa} + B(\xi,\kappa,\eta)\frac{\partial \sigma_{yy}}{\partial \eta} + C(\xi,\kappa)\frac{\partial \sigma_{yz}}{\partial \eta} + f_y, \tag{10}$$

$$\rho \frac{\partial w}{\partial t} = \frac{\partial \sigma_{xz}}{\partial \xi} + A(\xi,\kappa,\eta)\frac{\partial \sigma_{xz}}{\partial \eta} + \frac{\partial \sigma_{yz}}{\partial \kappa} + B(\xi,\kappa,\eta)\frac{\partial \sigma_{yz}}{\partial \eta} + C(\xi,\kappa)\frac{\partial \sigma_{zz}}{\partial \eta} + f_z, \tag{11}$$

$$\begin{aligned} \frac{\partial \sigma_{xx}}{\partial t} = {} & \Pi \frac{\tau_\varepsilon^P}{\tau_\sigma} \left(\frac{\partial u}{\partial \xi} + A(\xi,\kappa,\eta)\frac{\partial u}{\partial \eta} + \frac{\partial v}{\partial \kappa} + B(\xi,\kappa,\eta)\frac{\partial v}{\partial \eta} + C(\xi,\kappa)\frac{\partial w}{\partial \eta} \right) \\ & -2\mu \frac{\tau_\varepsilon^S}{\tau_\sigma} \left(\frac{\partial v}{\partial \kappa} + B(\xi,\kappa,\eta)\frac{\partial v}{\partial \eta} + C(\xi,\kappa)\frac{\partial w}{\partial \eta} \right) + r_{xx}, \end{aligned} \tag{12}$$

$$\begin{aligned} \frac{\partial \sigma_{yy}}{\partial t} = {} & \Pi \frac{\tau_\varepsilon^P}{\tau_\sigma} \left(\frac{\partial u}{\partial \xi} + A(\xi,\kappa,\eta)\frac{\partial u}{\partial \eta} + \frac{\partial v}{\partial \kappa} + B(\xi,\kappa,\eta)\frac{\partial v}{\partial \eta} + C(\xi,\kappa)\frac{\partial w}{\partial \eta} \right) \\ & -2\mu \frac{\tau_\varepsilon^S}{\tau_\sigma} \left(\frac{\partial u}{\partial \xi} + A(\xi,\kappa,\eta)\frac{\partial u}{\partial \eta} + C(\xi,\kappa)\frac{\partial w}{\partial \eta} \right) + r_{yy}, \end{aligned} \tag{13}$$

$$\frac{\partial \sigma_{zz}}{\partial t} = \Pi \frac{\tau_\varepsilon^P}{\tau_\sigma}\left(\frac{\partial u}{\partial \xi} + A(\xi,\kappa,\eta)\frac{\partial u}{\partial \eta} + \frac{\partial v}{\partial \kappa} + B(\xi,\kappa,\eta)\frac{\partial v}{\partial \eta} + C(\xi,\kappa)\frac{\partial w}{\partial \eta}\right)$$
$$-2\mu\frac{\tau_\varepsilon^S}{\tau_\sigma}\left(\frac{\partial u}{\partial \xi} + A(\xi,\kappa,\eta)\frac{\partial u}{\partial \eta} + \frac{\partial v}{\partial \kappa} + B(\xi,\kappa,\eta)\frac{\partial v}{\partial \eta}\right) + r_{zz}, \tag{14}$$

$$\frac{\partial \sigma_{xy}}{\partial t} = \mu\frac{\tau_\varepsilon^S}{\tau_\sigma}\left(\frac{\partial u}{\partial \kappa} + B(\xi,\kappa,\eta)\frac{\partial u}{\partial \eta} + \frac{\partial v}{\partial \xi} + A(\xi,\kappa,\eta)\frac{\partial v}{\partial \eta}\right) + r_{xy}, \tag{15}$$

$$\frac{\partial \sigma_{xz}}{\partial t} = \mu\frac{\tau_\varepsilon^S}{\tau_\sigma}\left(C(\xi,\kappa)\frac{\partial u}{\partial \eta} + \frac{\partial w}{\partial \xi} + A(\xi,\kappa,\eta)\frac{\partial w}{\partial \eta}\right) + r_{xz}, \tag{16}$$

$$\frac{\partial \sigma_{yz}}{\partial t} = \mu\frac{\tau_\varepsilon^S}{\tau_\sigma}\left(C(\xi,\kappa)\frac{\partial v}{\partial \eta} + \frac{\partial w}{\partial \kappa} + B(\xi,\kappa,\eta)\frac{\partial w}{\partial \eta}\right) + r_{yz}, \tag{17}$$

$$\frac{\partial r_{xx}}{\partial t} = -\frac{1}{\tau_\sigma}\left\{r_{xx} + \Pi\left(\frac{\tau_\varepsilon^P}{\tau_\sigma} - 1\right)\left[\frac{\partial u}{\partial \xi} + A(\xi,\kappa,\eta)\frac{\partial u}{\partial \eta} + \frac{\partial v}{\partial \kappa} + B(\xi,\kappa,\eta)\frac{\partial v}{\partial \eta}\right.\right.$$
$$\left.\left. + C(\xi,\kappa)\frac{\partial w}{\partial \eta}\right] - 2\mu\left(\frac{\tau_\varepsilon^S}{\tau_\sigma} - 1\right)\left(\frac{\partial v}{\partial \kappa} + B(\xi,\kappa,\eta)\frac{\partial v}{\partial \eta} + C(\xi,\kappa)\frac{\partial w}{\partial \eta}\right)\right\}, \tag{18}$$

$$\frac{\partial r_{yy}}{\partial t} = -\frac{1}{\tau_\sigma}\left\{r_{yy} + \Pi\left(\frac{\tau_\varepsilon^P}{\tau_\sigma} - 1\right)\left[\frac{\partial u}{\partial \xi} + A(\xi,\kappa,\eta)\frac{\partial u}{\partial \eta} + \frac{\partial v}{\partial \kappa} + B(\xi,\kappa,\eta)\frac{\partial v}{\partial \eta}\right.\right.$$
$$\left.\left. + C(\xi,\kappa)\frac{\partial w}{\partial \eta}\right] - 2\mu\left(\frac{\tau_\varepsilon^S}{\tau_\sigma} - 1\right)\left(\frac{\partial u}{\partial \xi} + A(\xi,\kappa,\eta)\frac{\partial u}{\partial \eta} + C(\xi,\kappa)\frac{\partial w}{\partial \eta}\right)\right\}, \tag{19}$$

$$\frac{\partial r_{zz}}{\partial t} = -\frac{1}{\tau_\sigma}\left\{r_{zz} + \Pi\left(\frac{\tau_\varepsilon^P}{\tau_\sigma} - 1\right)\left[\frac{\partial u}{\partial \xi} + A(\xi,\kappa,\eta)\frac{\partial u}{\partial \eta} + \frac{\partial v}{\partial \kappa} + B(\xi,\kappa,\eta)\frac{\partial v}{\partial \eta}\right.\right.$$
$$\left. + C(\xi,\kappa)\frac{\partial w}{\partial \eta}\right]$$
$$\left. - 2\mu\left(\frac{\tau_\varepsilon^S}{\tau_\sigma} - 1\right)\left(\frac{\partial u}{\partial \xi} + A(\xi,\kappa,\eta)\frac{\partial u}{\partial \eta} + \frac{\partial v}{\partial \kappa} + B(\xi,\kappa,\eta)\frac{\partial v}{\partial \eta}\right)\right\}, \tag{20}$$

$$\frac{\partial r_{xy}}{\partial t} = -\frac{1}{\tau_\sigma}\left\{r_{xy} + \mu\left(\frac{\tau_\varepsilon^S}{\tau_\sigma} - 1\right)\left(\frac{\partial u}{\partial \kappa} + B(\xi,\kappa,\eta)\frac{\partial u}{\partial \eta} + \frac{\partial v}{\partial \xi} + A(\xi,\kappa,\eta)\frac{\partial v}{\partial \eta}\right)\right\}, \tag{21}$$

$$\frac{\partial r_{xz}}{\partial t} = -\frac{1}{\tau_\sigma}\left\{r_{xz} + \mu\left(\frac{\tau_\varepsilon^S}{\tau_\sigma} - 1\right)\left(C(\xi,\kappa)\frac{\partial u}{\partial \eta} + \frac{\partial w}{\partial \xi} + A(\xi,\kappa,\eta)\frac{\partial w}{\partial \eta}\right)\right\}, \tag{22}$$

$$\frac{\partial r_{yz}}{\partial t} = -\frac{1}{\tau_\sigma}\left\{r_{yz} + \mu\left(\frac{\tau_\varepsilon^S}{\tau_\sigma} - 1\right)\left(C(\xi,\kappa)\frac{\partial v}{\partial \eta} + \frac{\partial w}{\partial \kappa} + B(\xi,\kappa,\eta)\frac{\partial w}{\partial \eta}\right)\right\}. \tag{23}$$

where ρ is the density, Π is the relaxation modulus for P–waves, $\Pi = \lambda + 2\mu$ (λ and μ are the Lamé parameters), and μ is the relaxation modulus for S–waves as in the elastic case. τ_ε^P and τ_ε^S are the strain relaxation times for P– and S–waves respectively, and τ_σ is the stress relaxation time. The same τ_σ can be used both for P– and S–waves (Blanch et al., 1995). f_x, f_y and f_z are the components of the body forces, u, v and w are the particle velocity components, and σ_{xx}, σ_{yy}, σ_{zz}, σ_{xy}, σ_{xz} and σ_{yz} are the stress components. r_{xx}, r_{yy}, r_{zz}, r_{xy}, r_{xz} and r_{yz} are the components of the memory variables. These are the curved grid equations governing wave propagation in a linear isotropic viscoelastic medium and are the equations of motion, the stress–strain relation and the memory variable equations given in the rectangular (ξ,κ,η)–grid.

3 Free Surface Boundary Conditions

The boundary condition at any free surface is that the traction vector $\vec{T}$ vanishes,

$$\vec{T} \equiv \tau \cdot \vec{n} = 0, \tag{24}$$

i.e., in Cartesian coordinates,

$$\sigma_{ij} n_j \quad = \quad 0, \tag{25}$$

where τ is the stress tensor with components σ_{ij} and $\vec{n}$ is a normal vector to the local surface point with components n_j; $i, j = 1, 2, 3$. Any normal vector may be used, even though $\vec{T}$ is defined by the unit normal vector. In 3–D we can choose

$$\vec{n} = \left(-\frac{\partial z_0(\xi,\kappa)}{\partial \xi}, -\frac{\partial z_0(\xi,\kappa)}{\partial \kappa}, 1 \right)^T \quad = \quad (-h_x, -h_y, 1)^T, \tag{26}$$

with $h_x = \partial z_0(\xi,\kappa)/\partial\xi$ and $h_y = \partial z_0(\xi,\kappa)/\partial\kappa$; h being the elevation data function and ^{T} means transposed. Partially differentiating equation (25) with respect to time and using the given $\vec{n}$ yields

$$-h_x \frac{\partial \sigma_{xx}}{\partial t} - h_y \frac{\partial \sigma_{xy}}{\partial t} + \frac{\partial \sigma_{xz}}{\partial t} \quad = \quad 0, \tag{27}$$

$$-h_x \frac{\partial \sigma_{xy}}{\partial t} - h_y \frac{\partial \sigma_{yy}}{\partial t} + \frac{\partial \sigma_{yz}}{\partial t} \quad = \quad 0, \tag{28}$$

$$-h_x \frac{\partial \sigma_{xz}}{\partial t} - h_y \frac{\partial \sigma_{yz}}{\partial t} + \frac{\partial \sigma_{zz}}{\partial t} \quad = \quad 0, \tag{29}$$

with σ_{xx}, σ_{xy}, σ_{yy}, σ_{xz}, σ_{yz} and σ_{zz} being the stress components.

We now substitute the expressions for all time differentiated stresses from equations (12)–(17), noting that the limit of an elastic medium can be assumed at the surface (Robertsson, 1996). Therefore $\tau_\varepsilon \equiv \tau_\sigma$ both for P– and S–waves and the memory variables vanish, i.e. $r_{xx} = r_{xy} = r_{yy} = r_{xz} = r_{yz} = r_{zz} \equiv 0$. Then equations (27)–(29) become

$$\begin{aligned}
&-h_x (\lambda + 2\mu) \left(\frac{\partial u}{\partial \xi} + A(\xi,\kappa,\eta) \frac{\partial u}{\partial \eta} \right) - h_x \lambda \left(\frac{\partial v}{\partial \kappa} + B(\xi,\kappa,\eta) \frac{\partial v}{\partial \eta} + C(\xi,\kappa) \frac{\partial w}{\partial \eta} \right) \\
&-h_y \mu \left(\frac{\partial v}{\partial \xi} + A(\xi,\kappa,\eta) \frac{\partial v}{\partial \eta} + \frac{\partial u}{\partial \kappa} + B(\xi,\kappa,\eta) \frac{\partial u}{\partial \eta} \right) \\
&+\mu \left(\frac{\partial w}{\partial \xi} + A(\xi,\kappa,\eta) \frac{\partial w}{\partial \eta} + C(\xi,\kappa) \frac{\partial u}{\partial \eta} \right) = 0,
\end{aligned} \tag{30}$$

$$\begin{aligned}
&-h_x \mu \left(\frac{\partial v}{\partial \xi} + A(\xi,\kappa,\eta) \frac{\partial v}{\partial \eta} + \frac{\partial u}{\partial \kappa} + B(\xi,\kappa,\eta) \frac{\partial u}{\partial \eta} \right) \\
&-h_y \lambda \left(\frac{\partial u}{\partial \xi} + A(\xi,\kappa,\eta) \frac{\partial u}{\partial \eta} + C(\xi,\kappa) \frac{\partial w}{\partial \eta} \right) - h_y (\lambda + 2\mu) \left(\frac{\partial v}{\partial \kappa} + B(\xi,\kappa,\eta) \frac{\partial v}{\partial \eta} \right) \\
&+\mu \left(\frac{\partial w}{\partial \kappa} + B(\xi,\kappa,\eta) \frac{\partial w}{\partial \eta} + C(\xi,\kappa) \frac{\partial v}{\partial \eta} \right) = 0,
\end{aligned} \tag{31}$$

$$\begin{aligned}
&-h_x \mu \left(\frac{\partial w}{\partial \xi} + A(\xi,\kappa,\eta) \frac{\partial w}{\partial \eta} + C(\xi,\kappa) \frac{\partial u}{\partial \eta} \right) - h_y \mu \left(\frac{\partial w}{\partial \kappa} + B(\xi,\kappa,\eta) \frac{\partial w}{\partial \eta} + C(\xi,\kappa) \frac{\partial v}{\partial \eta} \right) \\
&+\lambda \left(\frac{\partial u}{\partial \xi} + A(\xi,\kappa,\eta) \frac{\partial u}{\partial \eta} + \frac{\partial v}{\partial \kappa} + B(\xi,\kappa,\eta) \frac{\partial v}{\partial \eta} \right) + (\lambda + 2\mu) C(\xi,\kappa) \frac{\partial w}{\partial \eta} = 0.
\end{aligned} \tag{32}$$

with u, v and w being the particle velocities and λ and μ the Lamé parameters. Using the properties from equations (6)–(8) valid at the surface,

$$A(\xi,\kappa,\eta) \quad = \quad -C(\xi,\kappa) h_x, \tag{33}$$

$$B(\xi,\kappa,\eta) \quad = \quad -C(\xi,\kappa) h_y, \tag{34}$$

and rearranging terms gives the following form of equations (30)–(32),

$$
\begin{aligned}
& \left[h_x^2\left(\lambda+2\mu\right)+\mu\left(1+h_y^2\right)\right]C(\xi,\kappa)\frac{\partial u}{\partial \eta}+h_x h_y\left(\lambda+\mu\right)C(\xi,\kappa)\frac{\partial v}{\partial \eta} \\
& -h_x\left(\lambda+\mu\right)C(\xi,\kappa)\frac{\partial w}{\partial \eta} \\
= \;& h_x\left(\lambda+2\mu\right)\frac{\partial u}{\partial \xi}+h_y\mu\frac{\partial v}{\partial \xi}-\mu\frac{\partial w}{\partial \xi}+h_y\mu\frac{\partial u}{\partial \kappa}+h_x\lambda\frac{\partial v}{\partial \kappa}, \qquad (35) \\
& h_x h_y\left(\lambda+\mu\right)C(\xi,\kappa)\frac{\partial u}{\partial \eta}+\left[\mu\left(1+h_x^2\right)+h_y^2\left(\lambda+2\mu\right)\right]C(\xi,\kappa)\frac{\partial v}{\partial \eta} \\
& -h_y\left(\lambda+\mu\right)C(\xi,\kappa)\frac{\partial w}{\partial \eta} \\
= \;& h_y\lambda\frac{\partial u}{\partial \xi}+h_x\mu\frac{\partial v}{\partial \xi}+h_x\mu\frac{\partial u}{\partial \kappa}+h_y\left(\lambda+2\mu\right)\frac{\partial v}{\partial \kappa}-\mu\frac{\partial w}{\partial \kappa}, \qquad (36) \\
& -h_x\left(\lambda+\mu\right)C(\xi,\kappa)\frac{\partial u}{\partial \eta}-h_y\left(\lambda+\mu\right)C(\xi,\kappa)\frac{\partial v}{\partial \eta} \\
& +\left[\left(\lambda+2\mu\right)+\mu\left(h_x^2+h_y^2\right)\right]C(\xi,\kappa)\frac{\partial w}{\partial \eta} \\
= \;& -\lambda\frac{\partial u}{\partial \xi}+h_x\mu\frac{\partial w}{\partial \xi}-\lambda\frac{\partial v}{\partial \kappa}+h_y\mu\frac{\partial w}{\partial \kappa}. \qquad (37)
\end{aligned}
$$

Equations (35)–(37) are exact 3–D boundary conditions for an arbitrary, smooth, free surface topography. They are not restricted to the F–D method or any other specific numerical discretization technique.

We introduce the definitions

$$
\begin{aligned}
\zeta &\equiv \frac{\lambda}{\lambda+2\mu}, && (38)\\
d &\equiv h_x=\frac{\partial z_0(\xi,\kappa)}{\partial \xi}=\tan\theta, && (39)\\
e &\equiv \cos\left[\arctan\left(d\right)\right]=\cos\theta, && (40)\\
f &\equiv \sin\left[\arctan\left(d\right)\right]=\sin\theta, && (41)\\
p &\equiv h_y e=\frac{\partial z_0(\xi,\kappa)}{\partial \kappa}e=\tan\phi, && (42)
\end{aligned}
$$

where θ and ϕ are rotation angles of the local topography with the horizontal. Multiplying equations (35)–(37) by $2/\left(\lambda+2\mu\right)$ and noting that

$$
\frac{\mu}{\lambda+2\mu}=\frac{\frac{1}{2}\left(\lambda+2\mu-\lambda\right)}{\lambda+2\mu} = \frac{1}{2}\left(1-\zeta\right), \qquad (43)
$$

and hence

$$
\frac{\lambda+\mu}{\lambda+2\mu}=\zeta+\frac{1}{2}\left(1-\zeta\right) = \frac{1}{2}\left(1+\zeta\right), \qquad (44)
$$

gives the boundary conditions (35)–(37) the form

$$\begin{aligned}
&\left[2d^2+(1-\zeta)\left(1+\frac{p^2}{e^2}\right)\right]C(\xi,\kappa)\frac{\partial u}{\partial \eta}+\frac{dp}{e}(1+\zeta)\,C(\xi,\kappa)\frac{\partial v}{\partial \eta}-d\,(1+\zeta)\,C(\xi,\kappa)\frac{\partial w}{\partial \eta}\\
=\;& 2d\frac{\partial u}{\partial \xi}+\frac{p}{e}(1-\zeta)\frac{\partial v}{\partial \xi}-(1-\zeta)\frac{\partial w}{\partial \xi}+\frac{p}{e}(1-\zeta)\frac{\partial u}{\partial \kappa}+2d\zeta\frac{\partial v}{\partial \kappa}, \qquad (45)\\
&\frac{dp}{e}(1+\zeta)\,C(\xi,\kappa)\frac{\partial u}{\partial \eta}+\left[(1-\zeta)\left(1+d^2\right)+2\frac{p^2}{e^2}\right]C(\xi,\kappa)\frac{\partial v}{\partial \eta}-\frac{p}{e}(1+\zeta)\,C(\xi,\kappa)\frac{\partial w}{\partial \eta}\\
=\;& 2\frac{p}{e}\zeta\frac{\partial u}{\partial \xi}+d\,(1-\zeta)\frac{\partial v}{\partial \xi}+d\,(1-\zeta)\frac{\partial u}{\partial \kappa}+2\frac{p}{e}\frac{\partial v}{\partial \kappa}-(1-\zeta)\frac{\partial w}{\partial \kappa}, \qquad (46)\\
&-d\,(1+\zeta)\,C(\xi,\kappa)\frac{\partial u}{\partial \eta}-\frac{p}{e}(1+\zeta)\,C(\xi,\kappa)\frac{\partial v}{\partial \eta}+\left[2+(1-\zeta)\left(d^2+\frac{p^2}{e^2}\right)\right]C(\xi,\kappa)\frac{\partial w}{\partial \eta}\\
=\;& -2\zeta\frac{\partial u}{\partial \xi}+d\,(1-\zeta)\frac{\partial w}{\partial \xi}-2\zeta\frac{\partial v}{\partial \kappa}+\frac{p}{e}(1-\zeta)\frac{\partial w}{\partial \kappa}. \qquad (47)
\end{aligned}$$

Appendix A shows that these conditions are equivalent with the boundary condition formulations derived in Hestholm (1999), i.e.

$$\begin{aligned}
&\frac{1}{e^2}\left(1+p^2\right)C(\xi,\kappa)\frac{\partial u}{\partial \eta}+\frac{d}{e^2}\left(1+p^2\right)C(\xi,\kappa)\frac{\partial w}{\partial \eta}\\
=\;& 2d\frac{\partial u}{\partial \xi}+\frac{p}{e}\frac{\partial v}{\partial \xi}+\left(d^2-1\right)\frac{\partial w}{\partial \xi}+\frac{p}{e}\frac{\partial u}{\partial \kappa}+\frac{dp}{e}\frac{\partial w}{\partial \kappa}, \qquad (48)\\
&-\frac{fp}{e^2}\left(1+p^2\right)C(\xi,\kappa)\frac{\partial u}{\partial \eta}+\frac{1}{e^2}\left(1+p^2\right)C(\xi,\kappa)\frac{\partial v}{\partial \eta}+\frac{p}{e}\left(1+p^2\right)C(\xi,\kappa)\frac{\partial w}{\partial \eta}\\
=\;& -2dfp\frac{\partial u}{\partial \xi}+d\left(1-p^2\right)\frac{\partial v}{\partial \xi}+2fp\frac{\partial w}{\partial \xi}+d\left(1-p^2\right)\frac{\partial u}{\partial \kappa}+2\frac{p}{e}\frac{\partial v}{\partial \kappa}+\left(p^2-1\right)\frac{\partial w}{\partial \kappa}, \qquad (49)\\
&\frac{d}{e^2}\left(1+p^2\right)C(\xi,\kappa)\frac{\partial u}{\partial \eta}+\frac{p}{e^3}\left(1+p^2\right)C(\xi,\kappa)\frac{\partial v}{\partial \eta}-\frac{1}{e^2}\left(1+p^2\right)C(\xi,\kappa)\frac{\partial w}{\partial \eta}\\
=\;& \left[\zeta\left(1+\frac{p^2}{e^2}\right)+d^2\right]\frac{\partial u}{\partial \xi}-\frac{dp}{e}(\zeta-1)\frac{\partial v}{\partial \xi}+d\,(\zeta-1)\frac{\partial w}{\partial \xi}\\
&-\frac{dp}{e}(\zeta-1)\frac{\partial u}{\partial \kappa}+\frac{1}{e^2}\left(\zeta+p^2\right)\frac{\partial v}{\partial \kappa}+\frac{p}{e}(\zeta-1)\frac{\partial w}{\partial \kappa}, \qquad (50)
\end{aligned}$$

again using definitions (8) and (38)–(42). Both forms (35)–(37) (alternatively (45)–(47)) and (48)–(50) are closed, exact systems of equations for the particle velocities at a surface topography. In the derivation of both forms $\mu \neq 0$ is assumed. This means that the conditions cannot be used exactly for acoustic cases. Neither can they be used for vertical subsections, since $\tan\theta$ and/or $\tan\phi$ then go to infinity. Under these constraints, both systems of equations are spatially unconditionally stable when discretized by second–order F–Ds. We show this fact in the next section for the set (48)–(50). For the set (35)–(37) this is easily shown for special cases $h_x = 0$ and $h_y = 0$. Therefore it is always true due to the fact that the determinant of a system of equations is invariant under rotation of the coordinate system. Our experiments show that the forms (35)–(37) and (48)–(50) exhibit the same numerical properties in simulations. The derivation of the new set (35)–(37) and its equivalence with the form (48)–(50) (Appendix A) serve mainly as a simpler derivation and a verification of the previous form. We use the form (48)–(50) for numerical examples in this paper.

4 Numerical Discretization

For numerical discretization of the viscoelastic wave equations (9)–(23), we refer to the corresponding section in Hestholm (1999). Eighth–order, cost–optimized F–D operators (Kindelan et al., 1990) are used for spatial differentiation; and we employ a staggered discretization stencil of the velocity–stress formulation of the viscoelastic wave equations. An advantage of using staggered grids is that we achieve one increased F–D order for the same operator

length. Another advantage is that we are able to define only the particle velocities at the free surface while we avoid defining stresses there. Second–order F–Ds are used to discretize the 3–D boundary conditions (48)–(50), whereas the F–D order increases by two with each grid point away from the free surface, up to eighth–order in the interior. For time–stepping we use the second–order leap–frog technique and an explicit version of the unconditionally stable Crank–Nicholson method. The latter is used for time propagating the memory variables.

The formulas used for the viscoelastic relaxation times τ_σ, τ_ϵ^P and τ_ϵ^S given specific values for Q_P, Q_S and central frequency f, are according to Hestholm (1999). The Qs are decreased using a linear taper towards a value of ~ 2 along the grid boundaries. The method of Cerjan et al. (1985) is added on top of this in 2/3 of the absorbing layer (closest to the boundary) with an absorption constant of 0.06. A linear taper of the relaxation times towards their boundary values was found to work better than a cosine taper, when adding the method of Cerjan et al. (1985) on top, even if a cosine taper worked better than a linear taper. The total thickness over which the damping procedure is employed is 30 grid points, corresponding to 2.5 times the wavelength of the source's central frequency. Simone and Hestholm (1998) performed a specific comparison and assessment of the methods of Cerjan et al. (1985) and Peng and Toksöz (1995). Renaut and Petersen (1989) performed a general assessment and evaluation of various absorbing boundary methods. Although viscoelastic absorption along grid boundaries is favorable over most absorbing boundary conditions, improved results can usually be achieved by combining viscoelastic damping with some other method, like the one by Higdon (1990), or in our case Cerjan et al. (1985).

Using definitions (38)–(42), we define

$$\gamma_{11} \equiv \frac{1}{e^2}, \quad \gamma_{12} \equiv 0, \quad \gamma_{13} \equiv \frac{d}{e^2}, \quad \gamma_{21} \equiv -\frac{fp}{e^2}, \quad \gamma_{22} \equiv \frac{1}{e^2}, \quad \gamma_{23} \equiv \frac{p}{e}, \tag{51}$$

$$\gamma_{31} \equiv -\frac{d}{e^2}, \quad \gamma_{32} \equiv -\frac{p}{e^3}, \quad \gamma_{33} \equiv \frac{1}{e^2}, \tag{52}$$

$$\alpha_{11} \equiv 2d, \quad \alpha_{12} \equiv \frac{p}{e}, \quad \alpha_{13} \equiv d^2 - 1, \tag{53}$$

$$\alpha_{21} \equiv -2dfp, \quad \alpha_{22} \equiv d\left(1 - p^2\right), \quad \alpha_{23} \equiv 2fp, \tag{54}$$

$$\alpha_{31} \equiv -\left[\zeta\left(1 + \frac{p^2}{e^2}\right) + d^2\right], \quad \alpha_{32} \equiv \frac{dp}{e}\left(\zeta - 1\right), \quad \alpha_{33} \equiv -d\left(\zeta - 1\right), \tag{55}$$

$$\beta_{11} \equiv \frac{p}{e}, \quad \beta_{12} \equiv 0, \quad \beta_{13} \equiv \frac{dp}{e}, \tag{56}$$

$$\beta_{21} \equiv d\left(1 - p^2\right), \quad \beta_{22} \equiv 2\frac{p}{e}, \quad \beta_{23} \equiv p^2 - 1, \tag{57}$$

$$\beta_{31} \equiv \frac{dp}{e}\left(\zeta - 1\right), \quad \beta_{32} \equiv -\frac{1}{e^2}\left(\zeta + p^2\right), \quad \beta_{33} \equiv -\frac{p}{e}\left(\zeta - 1\right). \tag{58}$$

Then the topography boundary conditions (48)–(50) can be written

$$\gamma\left(1 + p^2\right) C(\xi, \kappa) \begin{pmatrix} \partial u/\partial\eta \\ \partial v/\partial\eta \\ \partial w/\partial\eta \end{pmatrix} = \alpha \begin{pmatrix} \partial u/\partial\xi \\ \partial v/\partial\xi \\ \partial w/\partial\xi \end{pmatrix} + \beta \begin{pmatrix} \partial u/\partial\kappa \\ \partial v/\partial\kappa \\ \partial w/\partial\kappa \end{pmatrix}, \tag{59}$$

using definition (8) and where γ is the 3×3 matrix consisting of the elements γ_{lm}, with l row and m column indices, respectively; α is the 3×3 matrix consisting of the elements α_{lm}, and β is the 3×3 matrix consisting of the elements β_{lm}. We discretize the boundary condition (59) for the particle velocities at the surface by second–order, staggered F–Ds. Then the discretized version becomes

$$\begin{aligned} & \gamma\left(1 + p^2\right) C(\xi, \kappa) \frac{1}{dz} \begin{pmatrix} [u(i,j,k) - u(i,j,k-1)] \\ [v(i,j,k) - v(i,j,k-1)] \\ [w(i,j,k) - w(i,j,k-1)] \end{pmatrix} \\ = \; & \alpha \frac{1}{dx} \begin{pmatrix} [u(i,j,k-1) - u(i-1,j,k-1)] \\ [v(i,j,k-1) - v(i-1,j,k-1)] \\ [w(i,j,k-1) - w(i-1,j,k-1)] \end{pmatrix} \\ + \; & \beta \frac{1}{dy} \begin{pmatrix} [u(i,j,k-1) - u(i,j-1,k-1)] \\ [v(i,j,k-1) - v(i,j-1,k-1)] \\ [w(i,j,k-1) - w(i,j-1,k-1)] \end{pmatrix}, \end{aligned} \tag{60}$$

where k is taken to be the level of the surface topography; here k denotes the vertical index and i and j the first and second horizontal indices, respectively. dz is the vertical grid distance of the numerical mesh, whereas dx and dy are the first and second horizontal grid distances. $u(i,j,k-1)$, $v(i,j,k-1)$, $w(i,j,k-1)$, $u(i-1,j,k-1)$, $v(i-1,j,k-1)$, $w(i-1,j,k-1)$, $u(i,j-1,k-1)$, $v(i,j-1,k-1)$ and $w(i,j-1,k-1)$ are all known from calculations in the previous time step and computed from the medium equations. We solve this system with respect to $u(i,j,k)$, $v(i,j,k)$ and $w(i,j,k)$, which are the surface values of the particle velocities. This gives a closed, explicit system of equations with determinant

$$\begin{aligned} D &= [\det\,\gamma]\left(1+p^2\right)^3 C^3(\xi,\kappa) \\ &= \frac{1}{e^6}\left(1+p^2\right)^4\left(1+d^2\right) C^3(\xi,\kappa) \;>0 \;\; \forall\,\theta\forall\,\phi. \end{aligned} \tag{61}$$

This determinant is always positive for all slope angles θ and ϕ and its minimum value is $C^3(\xi,\kappa)$, which occurs for a plane surface. Therefore the solution of (60) is unconditionally stable. The spatial stability of system (60), discretizing boundary conditions (48–50) by second–order F–Ds, is more important than one may think. The reason is that the numerical dispersion error of the phase velocity of Rg–waves is the same regardless of the F–D operator order used or whether the pseudospectral method (Fornberg, 1988b) is used for spatial differentiation (Xu et al., 1999). Only modelling of body waves gain in accuracy when high–order F–D or pseudospectral methods are applied. Hence for Rg–waves the numerical dispersion can only be reduced by closer spatial sampling regardless of modelling order. Therefore the second–order F–D method may as well be used since it is the most cost–effective.

5 Scattering from a hill and from a depression

Figures 3 and 4 are snapshots of the vertical particle velocity component w along a plane surface containing a hill and a depression, respectively. A Ricker point source exciting both a P– and an S–wave is located at $x = 40$ and $y = 30$ km and has central frequency of 2.5 Hz. Both the hill and the depression are centered at $x = y = 30$ km and consist of half a sine wavelength in both the x and y directions. This geometry constitutes sharp boundaries at the edges of each feature as the analytical spatial derivatives of the topography are discontinuous at those locations. The width of both features in either direction is 2.4 km, as is the height of the hill, the depth of the depression, and the wavelength of the central frequency of the applied point source. The P– and S–wave velocities of the homogeneous medium is 6.0 and 3.46 km/s, respectively, and the density is 2000 kg/m^3. The viscoelastic Q–value is 250 for P– and 200 for S–waves, and the rectangular grid in each case has size $301 \times 301 \times 101$ with a uniform grid distance of 0.2 km, covering a domain of $60 \times 60 \times 20$ km^3. The propagation of the initial P– and S/Rg–waves from the point source for various times can be seen in Figures 3 and 4. Clearly, both wave types generate reflected P– and Rg–waves in both cases. Diffracted P–to–Rg is identified and distinguished from the diffracted Rg–to–P in the case of the hill (Figure 3). As seen in Figure 4, these two diffracted wave conversions almost join in the case of the depression. The reason is that the depression acts almost like a low-frequency filter, mostly letting through waves of lower frequency. This may also be seen in 2–D simulations performed (not shown), for which the diffracted waves through the trench also have a very weakened amplitude. This last effect is not seen in the present 3–D example. A likely reason is that wavefronts join after passing the 3–D depression on either side.

The two last snapshots for each simulation exhibit a circular wave pattern around the geometric feature, showing the Rg–to–Rg conversion clearly. In addition to the depression acting as a low–frequency filter, it is also noteworthy that the reflections from the Rg–wave are stronger from the depression than from the hill. Part of the reason for this is the accumulation of energy inside the hill with time. At the two last times of Figure 3, this energy apparently contains the strongest amplitudes of the plot. For the depression (see Figure 4) the strongest amplitudes remain in the original Rg–wavefront. From this it is clear that a depression may cause even stronger back–scattered amplitudes than a hill, whereas a hill builds up strong energy at its location not found at a depression. These aspects can be confirmed from Figures 5 and 6, which are seismograms for the simulation of the hill and depression of Figures 3 and 4, respectively. They show the vertical particle velocity component along a west–east oriented sensor line at $y = 30$ km starting at $x = 5$ and ending at $x = 55$ km, interspaced by 1 km. The source coincides with receiver 36. The P–to–P reflection in particular is seen to be stronger from the depression than from the hill. The lower frequencies of the waves diffracted beyond the depression as Rg (Figure 6) may also be seen, as well as an energy accumulation at the hill (Figure 5).

The seismograms of Figures 7 and 8 show the first horizontal particle velocity component u for the hill and the trench simulation, respectively. The sensors are aligned in the south–north direction at $x = 40$ km, starting at $y = 5$

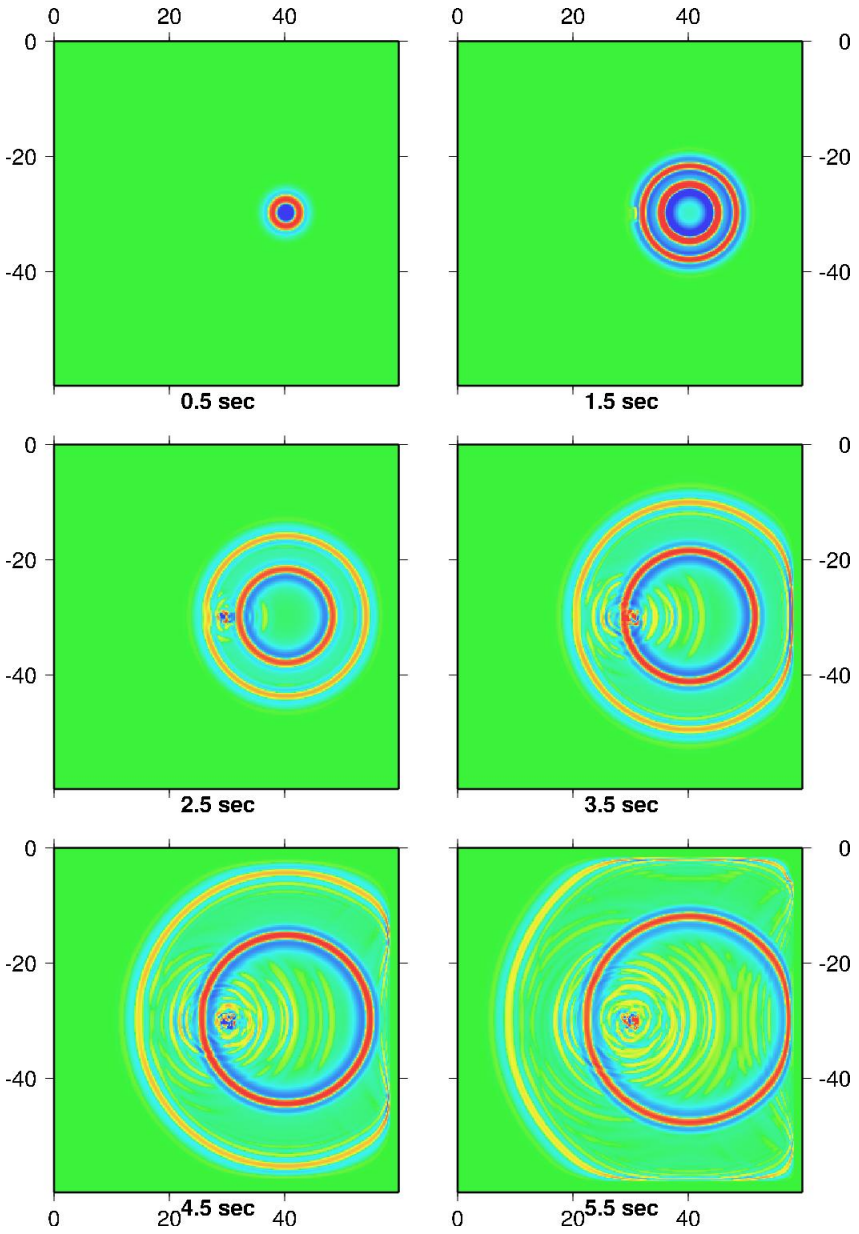

Figure 3: Snapshots of the vertical particle velocity component w at various times after a Ricker point source is released at $x = 40$ km and $y = 30$ km at the surface with a hill. The hill, centered at $x = y = 30$ km, is half a sine wavelength in both the x– and y–directions and has width of 2.4 km in both directions. This is also the height of the hill as well as the wavelength of the central frequency of the applied source. The snapshots of the viscoelastic simulation are taken along the surface of the $60 \times 60 \times 20$ km^3 homogeneous medium. Q is 250 for P– and 200 for S–waves, $v_p = 6$ km/s, $v_s = 3.46$ km/s and the density is 2000 kg/cm^3.

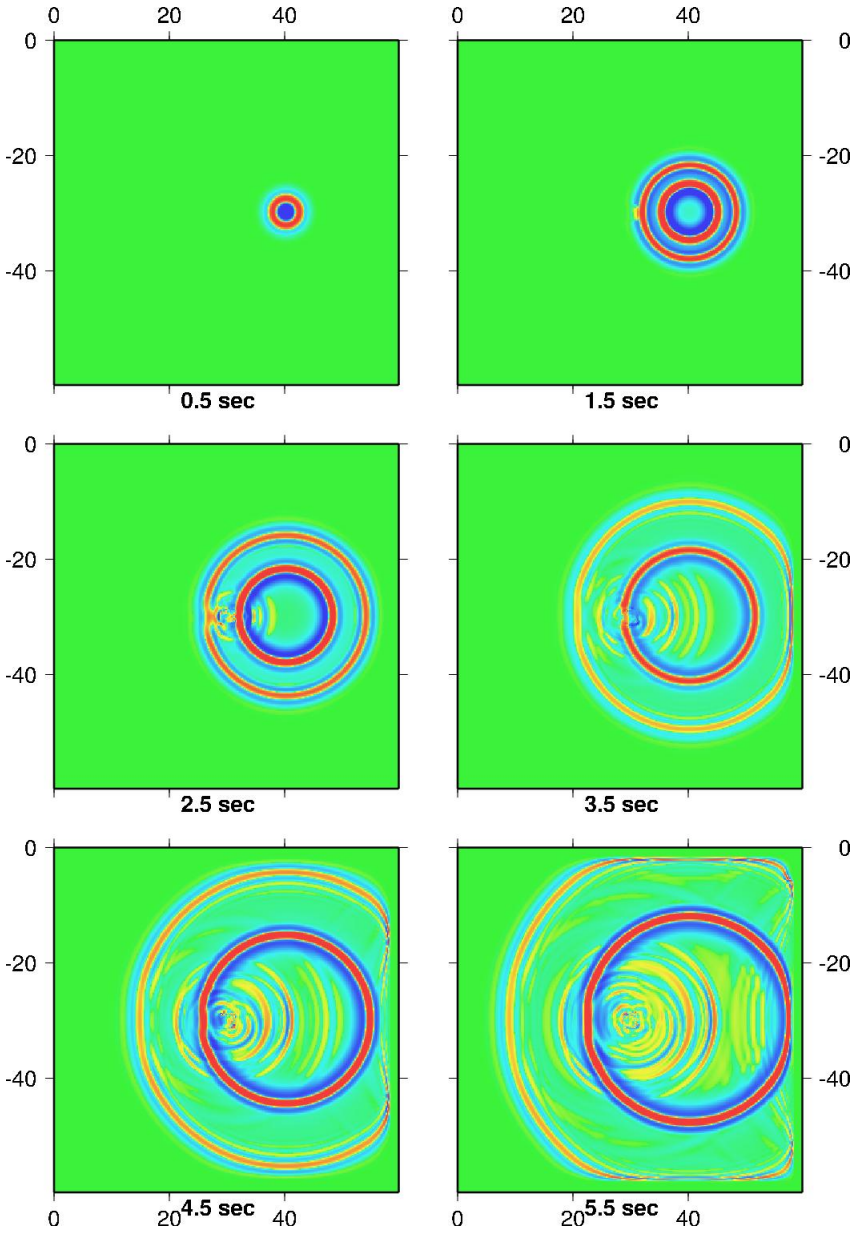

Figure 4: Snapshots of the vertical particle velocity component w at various times after a Ricker point source is released at $x = 40$ km and $y = 30$ km at the surface with a depression. The depression, centered at $x = y = 30$ km, is half a sine wavelength in both the x– and y–directions and has width of 2.4 km in both directions. This is also the depth of the depression as well as the wavelength of the central frequency of the applied source. The snapshots of the viscoelastic simulation are taken along the surface of the $60 \times 60 \times 20$ km^3 homogeneous medium. Q is 250 for P– and 200 for S–waves, $v_p = 6$ km/s, $v_s = 3.46$ km/s and the density is 2000 kg/cm^3.

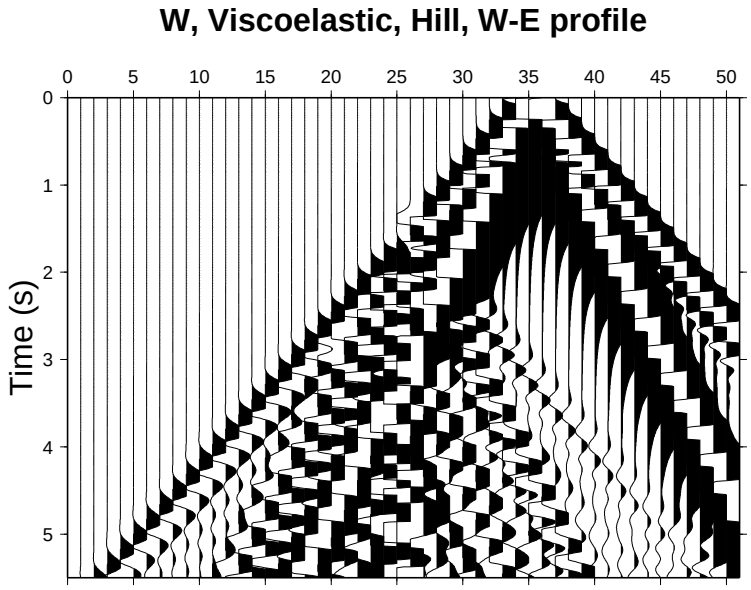

Figure 5: Seismogram of the vertical particle velocity component for the simulation of Figure 3. The receivers are aligned along a west–east oriented profile at $y = 30$ km starting at $x = 5$ km and ending at $x = 55$ km, interspaced by 1 km.

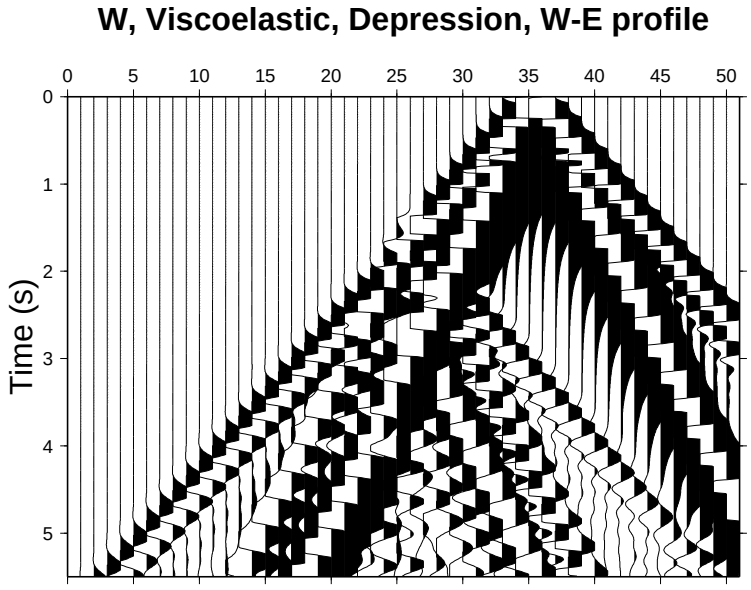

Figure 6: Seismogram of the vertical particle velocity component for the simulation of Figure 4. The receivers are aligned along a west–east oriented profile at $y = 30$ km, starting at $x = 5$ km and ending at $x = 55$ km, interspaced by 1 km.

and ending at $y = 55$ km, interspaced by 1 km. The source location is now at receiver 26. Apart from the outgoing P– and Rg–waves from the source, we see reflected P– and Rg–waves from the geometric features. The P–to–P reflection is confirmed to be much stronger from the depression (Figure 8) than from the hill (Figure 7). Interestingly, the first polarity of this reflection is negative for the depression and positive for the hill. We also confirm stronger amplitudes for later reflections from the depression than from the hill. The depression acts mainly to reflect waves whereas the hill acts mainly to trap and accumulate energy and at the same time releasing relatively short–period energy in all directions.

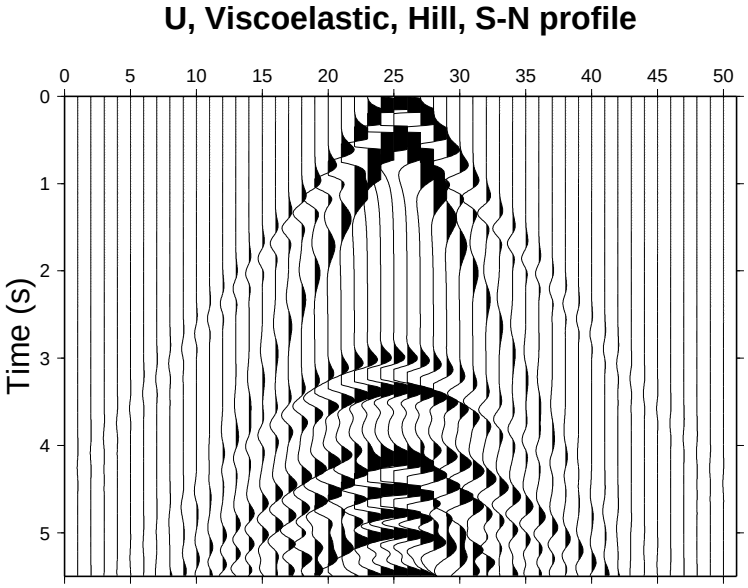

Figure 7: Seismogram of the first horizontal particle velocity component u for the simulation of Figure 3. The receivers are aligned along a south–north oriented profile at $x = 40$ km, starting at $y = 5$ km and ending at $y = 55$ km, interspaced by 1 km.

In this section, we investigated general 3–D effects from a hill and a trench, each with a circular shape (the same width as length). Bouchon et al. (1996) use the boundary element method in the wavenumber domain to investigate the effect on ground motion of a cosine–shaped hill with an elliptical base of ratio 2 to 1 at an otherwise plane surface of a homogeneous medium. They investigate only effects of incident S–waves, which are polarized in the longitudinal and transverse directions of the ellipse. Amplifications are found to be higher and stay higher for incident S–waves polarized along the transverse direction than they are for S–waves polarized along the longitudinal direction of the hill. Amplitude amplifications are consistently found to occur at and near the top of the hill over a broad range of frequencies. A strong directivity of scattered wavefield away from the topographic feature is also confirmed.

6 P– to Rg–Scattering from a Fjord Topography

Figure 9 represents a 200 × 100 km^2 area of elevation (upper map) and gradients (lower map) of a coastal area of topography from southwestern Norway with the city of Bergen at about x= 50, y= 50 km. Generally, elevation increases towards the east of the area with the steepest gradients centered around the middle of the west–east direction. The edges of the long and prominent Hardangerfjord incising the middle of the area from the south, contains the steepest and fastest varying gradients of the map. We simulate an initial dipping plane wave representing incident teleseismic P–waves towards the area. The plane wave is arriving from north–west and its incidence angle with the west–east direction (x–axis) is 1.79 degrees (negative slope value of 1/32); with the south–north direction (y–axis) it is 3.58

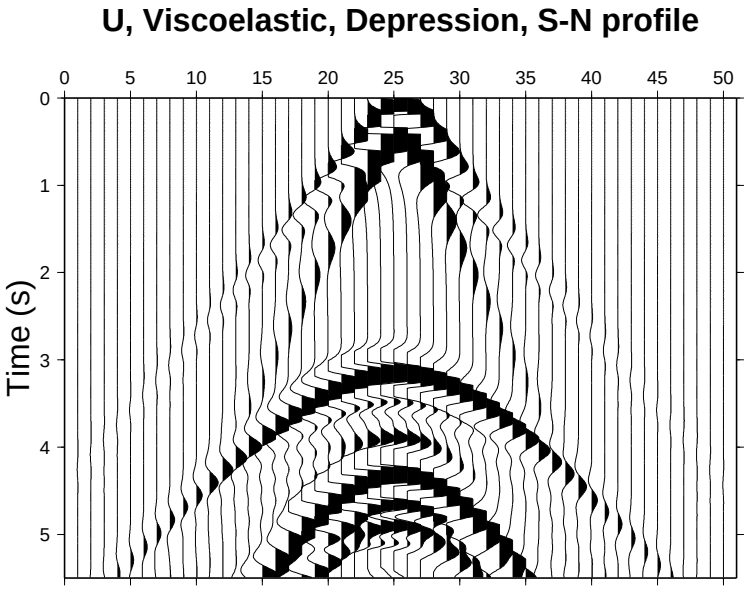

Figure 8: Seismogram of the first horizontal particle velocity component u for the simulation of Figure 4. The receivers are aligned along a south–north oriented profile at $x = 40$ km, starting at $y = 5$ km and ending at $y = 55$ km, interspaced by 1 km.

degrees (positive slope value of 1/16). This situation is shown in Figure 10 at 1.7 and 2.9 seconds of propagation time. The initial plane wave approaches the surface topography gradually with time and is implemented as a plane of Ricker source points with each source's central frequency equal to 2.5 Hz. The homogeneous medium has $v_P = 6.0$, $v_S = 3.46$ km/s, density 2000 kg/m^3, $Q_P = 250$ and $Q_S = 200$. A total grid size of $1000 \times 500 \times 150$ is used with a uniform grid sampling of 0.2 km, thus the model is 30 km deep. The total time simulated is 6.5 seconds. Message Passing Interface (MPI) was used to parallellize the program code by domain decomposition. The simulation took approximately 6 hours using a total of 8.1 GB on 32 processors on the parallel SGI (Cray) Origin 2000 machine located at Parallab, University of Bergen, Norway.

Figure 10 shows surface topography views of the development of the vertical particle velocity component across the coastal topography in intervals of 1.2 seconds. The procedure for absorption along grid boundaries is seen to work well. As mentioned, the medium is homogeneous, which means that the fjords and the sea are modeled as solid earth with the same medium properties as the rest of the model. Simulation of seismic/acoustic interfaces is possible using the program code with simpler media because, even if $\mu \neq 0$ is assumed in the derivation of the boundary conditions, we do not divide by μ anywhere in the numerical implementation. However, the complex fjord landscape of the present simulation leads to instabilities when applying high–order F–D operators across water–filled fjords.

The effects of the Hardangerfjord on the wavefield are clearly visible across the middle of the area in the south–north direction of Figure 10. We confirm that the steepest and roughest topography, as seen in the lower half of Figure 9, gives cause to the strongest wavefield amplitudes in Figure 10. This is verified from the broad south–north oriented complex wave band of strong amplitudes in Figure 10. Since plot scales are relative to amplitude strength, the strongest amplitudes of the simulation are displayed as clear blue/red contrasts, even if scattering exists in the entire domain with the exception of far west. A multiplicity of scattered waves can be observed; the ones that have propagated the longest distance are naturally located towards the north–west, since this is the direction from which the plane wave approaches. Circular wave patterns are confirmed around the locations of strongest gradients and topography variations.

Figure 11 shows the two next times of Figure 10. Here it is possible to follow the scattered waves from the previous snapshots with time and identify the strongest scattering sources as located close to and inside the sharp red and blue wavefronts. Scattering is caused solely by surface topography since the medium is homogeneous. Some grid boundary reflections are seen to interfere with the scattering in all snapshots. In this regard, the present situation of

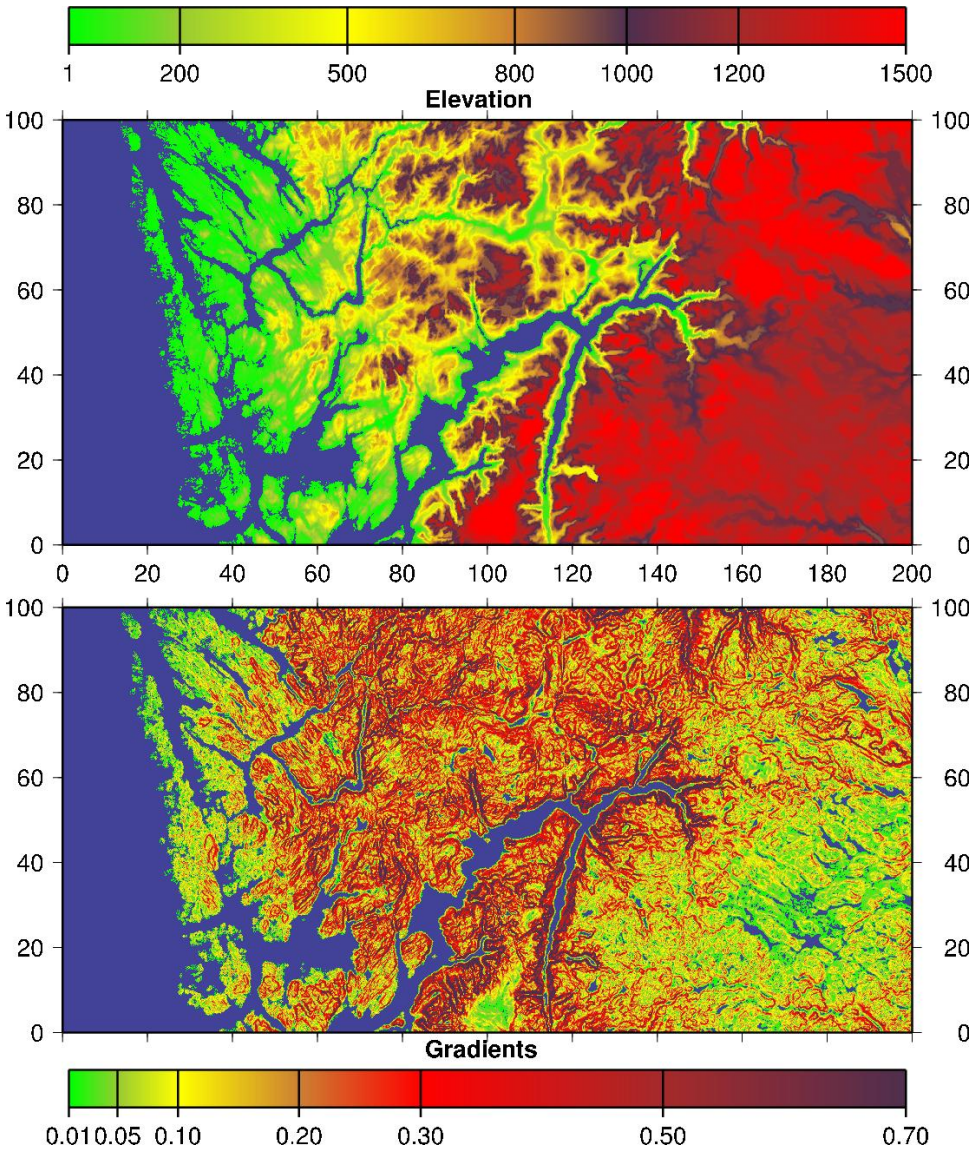

Figure 9: *Upper map:* Elevation data of the 200 × 100 × 30 km^3 domain used in the 3–D simulation. The seismogram receivers are interspaced by 1 km and located along two profiles from 76 to 125 km along the west–east (x) direction at y= 50 km and from 26 to 75 km along the south–north (y) direction at x= 100 km. Labels are in kilometers and blue represents zero values. *Lower map:* Gradients of the area; blue represents zero values.

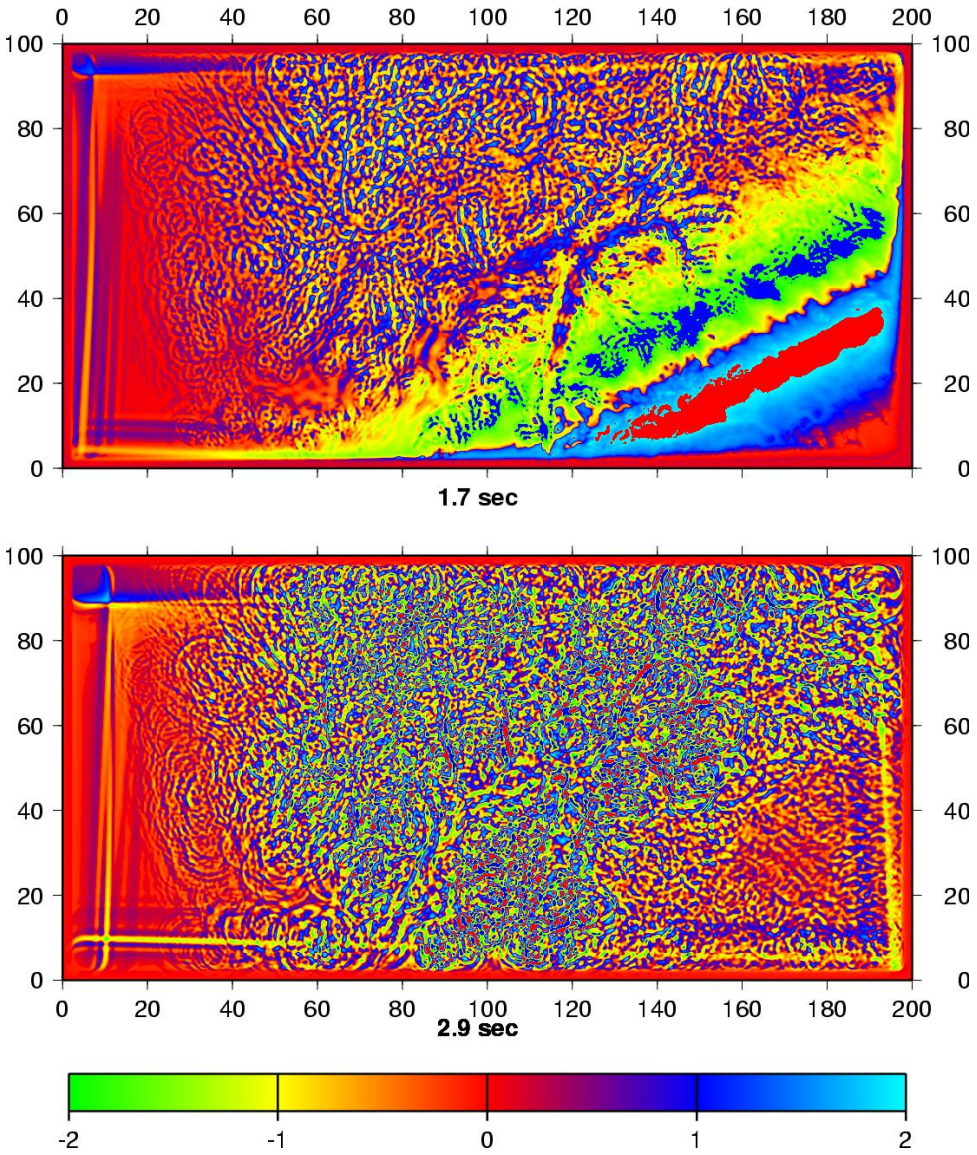

Figure 10: Snapshots of the vertical particle velocity component w at two times after a dipping plane wave is released close to the north–west corner of the surface topography of Figure 9. The dip of the plane wave is 1/32 in the negative x– and 1/16 in the positive y–direction. The snapshots of the viscoelastic simulation are taken along the surface topography of Figure 9 using a homogeneous medium of $Q_P = 250$, $Q_S = 200$, $v_p = 6$ km/s, $v_s = 3.46$ km/s and density 2000 kg/cm^3.

a plane wave reaching all grid edges is a worst case scenario because wave components in all directions reach all grid edges immediately. Even so, the example is included to illustrate the responses of the topography boundary condition implementation across the entire area.

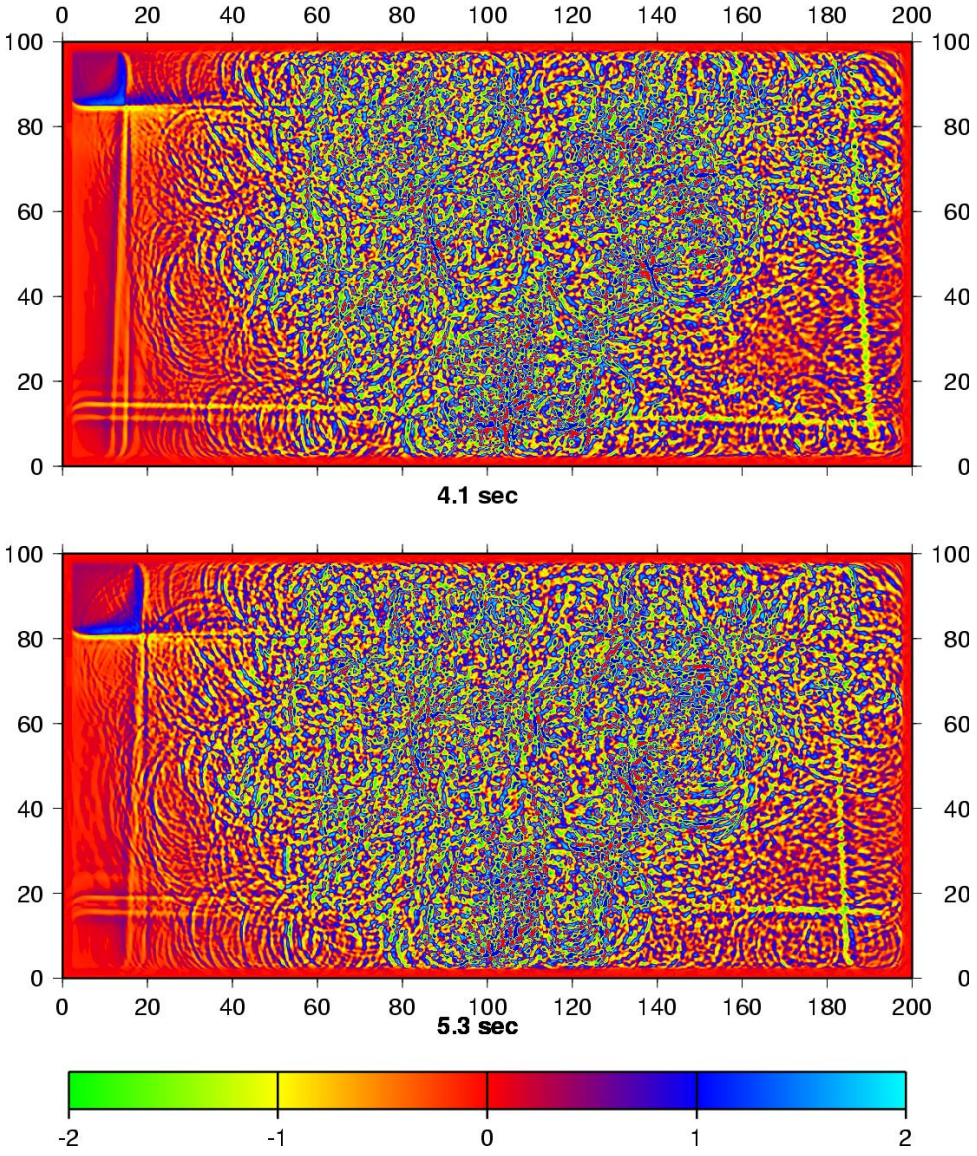

Figure 11: Next two snapshots for the simulation of Figure 10.

The parameters of this simulation are typical of teleseismic explosions and earthquakes, and lead snapshots and seismograms to exhibit no noticeable difference in appearance from corresponding elastic cases for the time simulated (Hestholm, 1999). Therefore, the predominant argument for viscoelastic rather than elastic modelling for low frequency simulations is the improved absorbing boundary conditions along the grid edges. For some types of random topography realizations, we even confirm stable viscoelastic runs where the exponential damping method of Cerjan et al. (1985), often employed in elastic modelling, leads to instabilities. The present viscoelastic wave modelling technique is a curved grid version of the formulation by Robertsson et al. (1994) with one relaxation mechanism. However, Xu and McMechan (1998, 1995) reduced the number of memory variables from seven to three by reparameterizing the wave equations, thereby reducing the total memory by 40 %.

Topography is the only cause for wave scattering in the homogeneous medium. A great amount of scattering is due

to out–of–plane effects from 3–D topography as 2–D synthetics lead to much simpler seismograms (Hestholm et al., 1999). Interestingly, a dipped plane wave gives rise to scattering of stronger amplitudes than a vertically incident (horizontal) plane wave (Hestholm, 1999). This reflects the significance of the orientation of the earthquake focal mechanism on local damages.

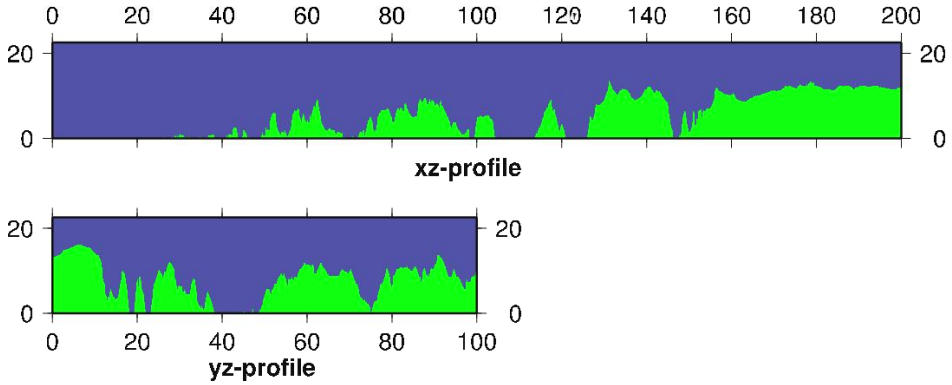

Figure 12: Vertically exaggerated (10 times) topographic west–east profile (upper plot) and south–north profile (lower plot), each at the middle of the domain covered by the surface of Figure 9. Horizontal axes are in kilometers and vertical axes are in 100 m.

Topography profiles across the model's west–east direction (upper part) and south–north direction (lower part) are shown in Figure 12. Each profile is taken at the middle point of the model. Horizontal axes are in kilometers and vertical axes are in 100 m, so in effect vertical axes are stretched ten times compared to horizontal ones, thus emphasizing topographic variations across the domain. Receivers are located from 76 to 125 km along the west–east profile and from 26 to 75 km along the south–north profile. Figure 13 shows seismograms of the vertical particle velocity component w in 50 receivers interspaced by 1 km along the west–east profile. Clearly, we see that the mountain from 75 to about 95 km generates a continuous and complex wavetrain of Rg–waves away from it. Except for the fjords, we see that along both topography profiles, the two features of strong gradients and topographic variations are coinciding, resulting in a complicated pattern of Rg–waves. There is also the presence of wavefield effects from nearby out–of–plane topographic features that enhance the seismogram's complex appearance. Fjords are seen to be the areas of least scattering and attenuate higher frequencies of scattered waves propagating towards them. In Figure 13 this is seen between receivers 30 and 40 and from 48 onwards. These effects may be compared with similar behaviour of the depression topography simulation in the previous section. Such features are also seen on the u and v components (not shown) in addition to even more complex wave pattern.

Figures 14 and 15 show seismograms along the south–north profile of Figure 12 (lower part) along 50 receivers interspaced by 1 km for the horizontal particle velocity components u and v, respectively. Both seismograms show complex scattering from the mountainous features; it is possible to identify these features as the sources of strongest amplitudes of incoherent scattering. Figure 14 shows the u–component which is the transverse component of the profile. Therefore, it is natural that this component is attenuated significantly in the fjord between 40 and 50 kilometers (between receivers 14 and 20), the fjord acting as a valley. In Figure 15 on the other hand, which is the parallel component v to the profile, we see that the strongly varying and complicated topographic features to the south of the fjord cause strong Rg–waves to propagate northwards into the fjord. Among all the out–of–plane effects, it may also be possible to track some Rg wavetrains emanating out of the two most prominent remaining peaks in the northward direction of this profile.

7 Conclusions

New exact boundary conditions for free surface topography on top of seismic media for wave propagation modelling have been derived and shown to be equivalent, both mathematically and numerically, with boundary condition formulations derived in earlier work. This verifies the validity of the formulations. We outline a numerical discretization by spatially second–order F-Ds of the boundary conditions, and show that the resulting system of equations for the free surface

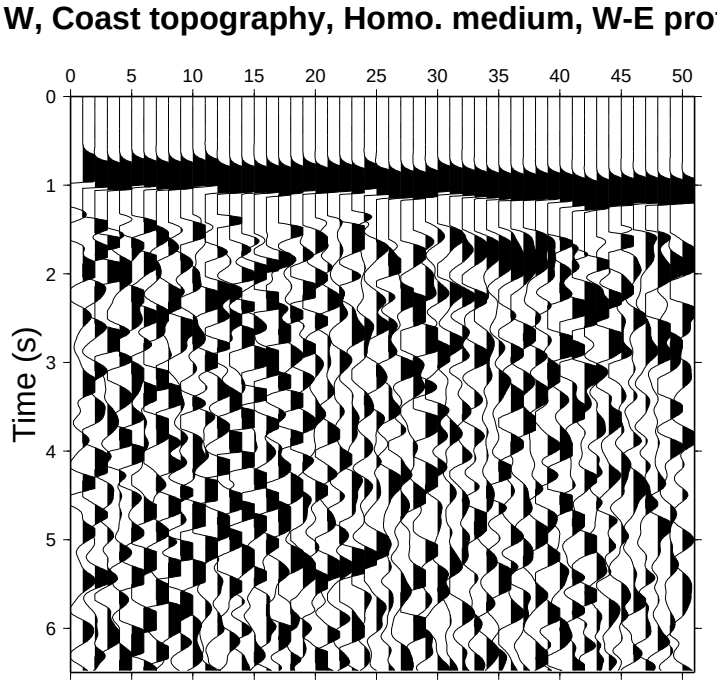

Figure 13: Seismogram of the vertical particle velocity component w for the viscoelastic simulation of Figures 10 and 11 along the west–east oriented profile of Figure 12. The receivers are located from 76 to 125 km and interspaced by 1 km.

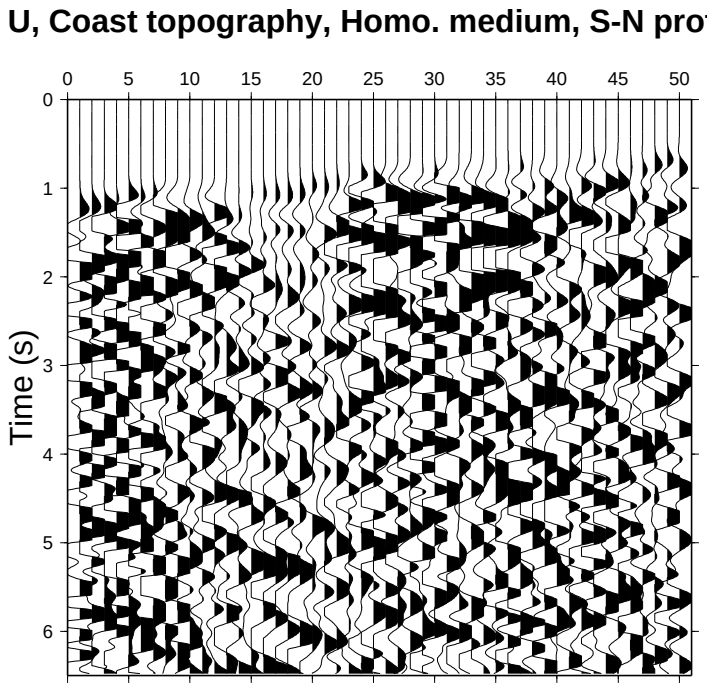

Figure 14: Seismogram of the horizontal particle velocity component u for the viscoelastic simulation of Figures 10 and 11 along the south–north oriented profile of Figure 12. The receivers are located from 26 to 75 km and interspaced by 1 km.

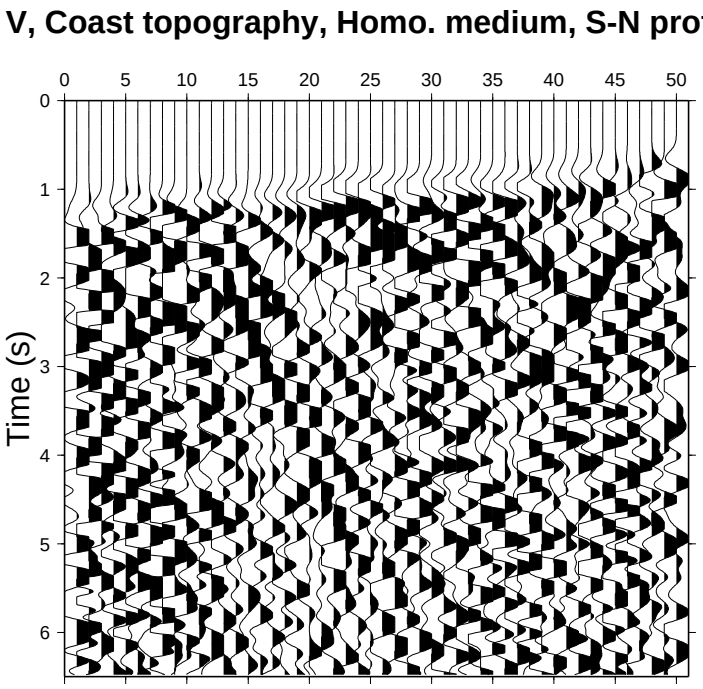

Figure 15: Seismogram of the horizontal particle velocity component v for the viscoelastic simulation of Figures 10 and 11 along the south–north oriented profile of Figure 12. The receivers are located from 26 to 75 km and interspaced by 1 km.

particle velocities is spatially unconditionally stable. The boundary conditions are used in this work to propagate waves in full viscoelastic media using the velocity–stress formulation of the wave equations for curved grids. Our implementation is applied to simulate scattering from topographic features. It generates accumulated short–period energy at a hill, which acts as a source of such energy in all directions as well as lower frequency waves diffracting through a depression. It also gives realistic scattering and complex wave pattern, due to out–of–plane effects from 3–D topography. P–to–Rg scattering from mountainous areas is synthesized for an incident dipping plane P–wavefront on a fjord landscape of southwestern Norway. Fjords, simulated as valleys, are seen to exhibit effects similar to a depression, i.e. attenuated higher frequency and amplified lower frequency transmitted and reflected waves. In earthquake and teleseismic simulations producing seismograms similar to elastic cases, viscoelastic low Q still produces superior absorbing boundaries. Many theoretical and numerical results consistently predict amplitude amplification at ridge crests, but often underestimate amplifications actually observed in the field. An explanation for this may be that these calculations assume 2–D topographic geometries, ignoring out–of–plane effects (Hestholm et al., 1999).

8 Acknowledgments

We greatly appreciate discussions with and support from Prof. Eystein Husebye (University of Bergen, Norway, Dept. of Solid Earth Physics) who also provided the topographic map of southwestern Norway, attained from the Norwegian Governmental Map Authorities. We thank Prof. Manik Talwani (Rice University) and Prof. George McMechan (University of Texas at Dallas) for support, as well as Liz Henderson (Earth Resources Laboratory, Massachusetts Institute of Technology) for useful comments to the manuscript. This research was supported by the Norwegian Research Council and by the Earth Resources Laboratory, Massachusetts Institute of Technology, both through post doctoral fellowships. The research was also supported by the Cold Regions Research and Engineering Laboratory, US Army Corps of Engineers, under contract DACA89-99-C-0002, and by the Norwegian Supercomputer Committee through a grant of computing time.

References

J. O. Blanch, J. O. A. Robertsson, and W. W. Symes. Modeling of a constant Q: Methodology and algorithm for an efficient and optimally inexpensive viscoelastic technique. *Geophysics*, 60:176–184, 1995.

M. Bouchon, C. A. Schultz, and M. N. Toksöz. Effect of three–dimensional topography on seismic motion. *J. Geophys. Res.*, 101:5835–5846, 1996.

J. M. Carcione, D. Kosloff, and R. Kosloff. Wave propagation simulation in a linear viscoelastic medium. *Geophys. J. Roy. Astr. Soc.*, 95:597–611, 1988.

C. Cerjan, D. Kosloff, R. Kosloff, and M. Reshef. A nonreflecting boundary condition for discrete acoustic and elastic wave equations. *Geophysics*, 50:705–708, 1985.

B. Fornberg. Generation of finite difference formulas on arbitrary spaced grids. *Mathematics of Computation*, 51:699–706, 1988a.

B. Fornberg. The pseudospectral method: Accurate representation of interfaces in elastic wave calculations. *Geophysics*, 53:625–637, 1988b.

S. O. Hestholm. 3–D finite difference viscoelastic wave modelling including surface topography. *Geophys. J. Int.*, 139:852–878, 1999.

S. O. Hestholm and B. O. Ruud. 2–D finite difference elastic wave modelling including surface topography. *Geophys. Prosp.*, 42:371–390, 1994.

S. O. Hestholm and B. O. Ruud. 3–D finite difference elastic wave modeling including surface topography. *Geophysics*, 63:613–622, 1998.

S. O. Hestholm, B. O. Ruud, and E. S. Husebye. 3–D versus 2–D finite difference seismic synthetics including real surface topography. *Physics of the Earth and Planetary Interiors*, 113:339–354, 1999.

R. L. Higdon. Radiation boundary conditions for elastic wave propagation. *SIAM J. of Num. Analysis*, 27: 831–870, 1990.

R. S. Jih, K. L. McLaughlin, and Z. A. Der. Free–boundary conditions of arbitrary topography in a two–dimensional explicit finite difference scheme. *Geophysics*, 53:1045–1055, 1988.

M. Kindelan, A. Kamel, and P. Sguazzero. On the construction and efficiency of staggered numerical differentiators for the wave equation. *Geophysics*, 55:107–110, 1990.

M. Komatitsch, F. Coutel, and P. Mora. Tensorial formulation of the wave equation for modelling curved interfaces. *Geophys. J. Int.*, 127:156–168, 1996.

A. R. Levander. Fourth–order finite–difference P–SV seismograms. *Geophysics*, 53:1425–1436, 1988.

T. Ohminato and B. A. Chouet. A free–surface boundary condition for including 3D topography in the finite difference method. *Bull. Seism. Soc. Am.*, 87:494–515, 1997.

C. Peng and M. N. Toksöz. An optimal absorbing boundary condition for elastic wave modeling. *Geophysics*, 60:296–301, 1995.

R. A. Renaut and J. Petersen. Stability of wide–angle absorbing boundary conditions for the wave equation. *Geophysics*, 54:1153–1163, 1989.

J. O. A. Robertsson. A numerical free–surface condition for elastic/viscoelastic finite–difference modeling in the presence of topography. *Geophysics*, 61:1921–1934, 1996.

J. O. A. Robertsson, J. O. Blanch, and W. W. Symes. Viscoelastic finite–difference modeling. *Geophysics*, 59:1444–1456, 1994.

F. J. Sanchez-Sesma and M. Campillo. Diffraction of P, SV, and Rayleigh waves by topographic features: A boundary integral formulation. *Bull. Seism. Soc. Am.*, 81:2234–2253, 1991.

A. Simone and S. Hestholm. Instabilities in applying absorbing boundary conditions to high order seismic modeling algorithms. *Geophysics*, 63:1017–1023, 1998.

E. Tessmer and D. Kosloff. 3–D elastic modeling with surface topography by a Chebychev spectral method. *Geophysics*, 59:464–473, 1994.

E. Tessmer, D. Kosloff, and A. Behle. Elastic wave propagation simulation in the presence of surface topography. *Geophys. J. Int.*, 108:621–632, 1992.

J. Virieux. P-SV wave propagation in heterogeneous media: Velocity–stress finite–difference method. *Geophysics*, 51:889–901, 1986.

H. Xu, S. M. Day, and J.-B. H. Minster. Two-dimensional linear and nonlinear wave propagation in a half-space. *Bull. Seism. Soc. Am.*, 89:903–917, 1999.

T. Xu and G. A. McMechan. Composite memory variables for viscoelastic synthetic seismograms. *Geophys. J. Int.*, 121:634–639, 1995.

T. Xu and G. A. McMechan. Efficient 3–D viscoelastic modeling with application to near–surface land seismic data. *Geophysics*, 63:601–612, 1998.

A Equivalence of boundary condition formulations

Using definitions (38)–(42) and

$$q \equiv \cos\left[\arctan\left(p\right)\right] = \cos\phi, \tag{62}$$
$$r \equiv \sin\left[\arctan\left(p\right)\right] = \sin\phi, \tag{63}$$

where ϕ is the second rotation angle of the local topography, we multiply the last of the new boundary condition formulations, equation (47), by d and add the result to the first equation (45). After a little contraction and factorization this gives

$$\begin{aligned} &\left[d^2\left(1-\zeta\right)+\left(1+\frac{p^2}{e^2}\right)\left(1-\zeta\right)\right]C(\xi,\kappa)\frac{\partial u}{\partial \eta} \\ &+d\left[\left(1+d^2\right)\left(1-\zeta\right)+\frac{p^2}{e^2}\left(1-\zeta\right)\right]C(\xi,\kappa)\frac{\partial w}{\partial \eta} \\ = \;& \left(1-\zeta\right)\left[2d\frac{\partial u}{\partial \xi}+\frac{p}{e}\frac{\partial v}{\partial \xi}+\left(d^2-1\right)\frac{\partial w}{\partial \xi}+\frac{p}{e}\frac{\partial u}{\partial \kappa}+\frac{dp}{e}\frac{\partial w}{\partial \kappa}\right]. \end{aligned} \tag{64}$$

Using the trigonometric identity

$$d^2+1+\frac{p^2}{e^2}=\frac{1}{e^2}+\frac{p^2}{e^2} \quad = \quad \frac{1}{e^2}\left(1+p^2\right), \tag{65}$$

and dividing through by $1-\zeta$ (thereby assuming $\mu \neq 0$), gives equation (48).

To arrive at equation (49) from equations (45)–(47), we multiply equation (47) by ep, add equation (46), and subtract equation (45) after multiplying it by dep; in other words $ep\times$(47) + (46) − $dep\times$(45), where the numbers

refer to equations. This gives, after some terms cancel,

$$\begin{aligned}
&\left(-2dep+\frac{dp}{e}\zeta+\frac{dp}{e}-2d^3ep-\frac{d}{e}p^3+\frac{d}{e}p^3\zeta\right)C(\xi,\kappa)\frac{\partial u}{\partial\eta}\\
&+\left(-p^2-p^2\zeta+d^2-d^2\zeta+1-\zeta+2\frac{p^2}{e^2}-d^2p^2-d^2p^2\zeta\right)C(\xi,\kappa)\frac{\partial v}{\partial\eta}\\
&+\left(2ep+2d^2ep+\frac{p^3}{e}-\frac{p^3}{e}\zeta-\frac{p}{e}-\frac{p}{e}\zeta\right)C(\xi,\kappa)\frac{\partial w}{\partial\eta}\\
=\;&\left(-2ep\zeta+2\frac{p}{e}\zeta-2d^2ep\right)\frac{\partial u}{\partial\xi}+\left(d-d\zeta-dp^2+dp^2\zeta\right)\frac{\partial v}{\partial\xi}+\left(2dep-2dep\zeta\right)\frac{\partial w}{\partial\xi}\\
&+\left(d-d\zeta-dp^2+dp^2\zeta\right)\frac{\partial u}{\partial\kappa}+\left(-2ep\zeta+2\frac{p}{e}-2d^2ep\zeta\right)\frac{\partial v}{\partial\kappa}\\
&+\left(p^2-p^2\zeta-1+\zeta\right)\frac{\partial w}{\partial\kappa}. \qquad (66)
\end{aligned}$$

Now we simplify each of the coefficients by using trigonometric identities. For the coefficient of $C(\xi,\kappa)\partial u/\partial\eta$:

$$\begin{aligned}
&dep\left(-2+\frac{1}{e^2}\zeta+\frac{1}{e^2}-2d^2-\frac{p^2}{e^2}+\frac{p^2}{e^2}\zeta\right)\\
=\;&fp\left[-2\left(1+d^2\right)+\frac{1}{e^2}\left(1-p^2+\zeta+p^2\zeta\right)\right]\\
=\;&\frac{fp}{e^2}\left[-2+1-p^2+\zeta\left(1+p^2\right)\right]=-\frac{fp}{e^2}\left[\left(1+p^2\right)\left(1-\zeta\right)\right], \qquad (67)
\end{aligned}$$

noting that $1+d^2=1/e^2$ and $de=f$. For the coefficient of $C(\xi,\kappa)\partial v/\partial\eta$:

$$\begin{aligned}
&-p^2\left(1+d^2+\zeta+d^2\zeta-\frac{2}{e^2}\right)+\left(1-\zeta\right)\left(1+d^2\right)\\
=\;&-p^2\left[\left(1+d^2\right)\left(1+\zeta\right)-\frac{2}{e^2}\right]+\left(1-\zeta\right)\left(1+d^2\right)=-p^2\left(\frac{1}{e^2}+\frac{\zeta}{e^2}-\frac{2}{e^2}\right)+\left(1-\zeta\right)\frac{1}{e^2}\\
=\;&-\frac{p^2}{e^2}\left(-1+\zeta\right)+\frac{1}{e^2}\left(1-\zeta\right)=\frac{1}{e^2}\left(1+p^2\right)\left(1-\zeta\right). \qquad (68)
\end{aligned}$$

For the coefficient of $C(\xi,\kappa)\partial w/\partial\eta$:

$$\begin{aligned}
&\frac{p}{e}\left(2e^2+2d^2e^2+p^2-p^2\zeta-1-\zeta\right)=\frac{p}{e}\left[2e^2+2f^2+p^2\left(1-\zeta\right)-1-\zeta\right]\\
=\;&\frac{p}{e}\left(1+p^2\right)\left(1-\zeta\right). \qquad (69)
\end{aligned}$$

For the coefficient of $\partial u/\partial\xi$:

$$\begin{aligned}
&-2dfp\left(\frac{e\zeta}{df}-\frac{\zeta}{def}+\frac{de}{f}\right)=-2dfp\left(\frac{\zeta}{d^2}-\frac{\zeta}{f^2}+1\right)=-2dfp\left[\zeta\left(\frac{e^2-1}{f^2}\right)+1\right]\\
=\;&-2dfp\left(1-\zeta\right). \qquad (70)
\end{aligned}$$

For the coefficient of $\partial v/\partial\xi$:

$$d\left(1-\zeta\right)-dp^2\left(1-\zeta\right)=d\left(1-p^2\right)\left(1-\zeta\right). \qquad (71)$$

For the coefficient of $\partial w/\partial\xi$:

$$2dep-2dep\zeta=2fp\left(1-\zeta\right). \qquad (72)$$

For the coefficient of $\partial u/\partial\kappa$:

$$d\left[\left(1-p^2\right)-\zeta+p^2\zeta\right]=d\left(1-p^2\right)\left(1-\zeta\right). \qquad (73)$$

For the coefficient of $\partial v/\partial\kappa$:

$$2\frac{p}{e}\left(1-e^2\zeta-d^2e^2\zeta\right)=2\frac{p}{e}\left[1-\zeta\left(e^2+f^2\right)\right]=2\frac{p}{e}\left(1-\zeta\right). \tag{74}$$

For the coefficient of $\partial w/\partial\kappa$:

$$p^2-p^2\zeta-1+\zeta=\left(p^2-1\right)\left(1-\zeta\right). \tag{75}$$

The equation resulting from these trigonometric simplifications we divide through by $1-\zeta$, giving equation (49).

To get equation (50) from equations (45)–(47), we take equation (47), subtract $d\times$ equation (45) before subtracting $p/e\times$ equation (46); in other words (47) $-$ $d\times$(45) $-$ $p/e\times$(46). This gives

$$\begin{aligned}
& d\left[-\zeta-1-2d^2-\left(1+\frac{p^2}{e^2}\right)\left(1-\zeta\right)-\frac{p^2}{e^2}\zeta-\frac{p^2}{e^2}\right]C(\xi,\kappa)\frac{\partial u}{\partial\eta}\\
& +\frac{p}{e}\left[-\zeta-1-d^2\zeta-d^2-\left(1+d^2\right)\left(1-\zeta\right)-2\frac{p^2}{e^2}\right]C(\xi,\kappa)\frac{\partial v}{\partial\eta}\\
& +\left[2+\left(d^2+\frac{p^2}{e^2}\right)\left(1-\zeta\right)+d^2\zeta+d^2+\frac{p^2}{e^2}\zeta+\frac{p^2}{e^2}\right]C(\xi,\kappa)\frac{\partial w}{\partial\eta}\\
= \;& \left(-2\zeta-2d^2-2\frac{p^2}{e^2}\zeta\right)\frac{\partial u}{\partial\xi}-2\frac{dp}{e}\left(1-\zeta\right)\frac{\partial v}{\partial\xi}+2d\left(1-\zeta\right)\frac{\partial w}{\partial\xi}\\
& -2\frac{dp}{e}\left(1-\zeta\right)\frac{\partial u}{\partial\kappa}+\left(-2\zeta-2d^2\zeta-2\frac{p^2}{e^2}\right)\frac{\partial v}{\partial\kappa}+2\frac{p}{e}\left(1-\zeta\right)\frac{\partial w}{\partial\kappa}.
\end{aligned} \tag{76}$$

We perform the following trigonometric simplifications. For the coefficient of $C(\xi,\kappa)\partial u/\partial\eta$:

$$\begin{aligned}
& d\left[\left(1+\frac{p^2}{e^2}\right)\left(\zeta-1\right)-\zeta\left(1+\frac{p^2}{e^2}\right)-\left(1+\frac{p^2}{e^2}+2d^2\right)\right]\\
= \;& d\left[\zeta\left(1+\frac{p^2}{e^2}\right)-\left(1+\frac{p^2}{e^2}\right)-\zeta\left(1+\frac{p^2}{e^2}\right)-\left(1+\frac{p^2}{e^2}\right)-2d^2\right]\\
= \;& -2d\left(1+\frac{p^2}{e^2}+d^2\right)=-2\frac{d}{e^2}\left(1+p^2\right).
\end{aligned} \tag{77}$$

For the coefficient of $C(\xi,\kappa)\partial v/\partial\eta$:

$$\begin{aligned}
& \frac{p}{e}\left[-\left(1+d^2\right)\left(1+\zeta\right)-\left(1+d^2\right)\left(1-\zeta\right)-2\frac{p^2}{e^2}\right]\\
= \;& \frac{p}{e}\left[-\left(1+d^2\right)\left(1+\zeta+1-\zeta\right)-2\frac{p^2}{e^2}\right]=-2\frac{p}{e}\left(1+d^2+\frac{p^2}{e^2}\right)\\
= \;& -2\frac{p}{e}\frac{1}{e^2}\left(1+p^2\right)=-2\frac{p}{e^3}\left(1+p^2\right).
\end{aligned} \tag{78}$$

For the coefficient of $C(\xi,\kappa)\partial w/\partial\eta$:

$$\begin{aligned}
& \left[2+\left(d^2+\frac{p^2}{e^2}\right)\left(1-\zeta\right)+\left(d^2+\frac{p^2}{e^2}\right)\left(\zeta+1\right)\right]\\
= \;& 2+\left(d^2+\frac{p^2}{e^2}\right)\left(1-\zeta+\zeta+1\right)=2\left(1+d^2+\frac{p^2}{e^2}\right)=\frac{2}{e^2}\left(1+p^2\right).
\end{aligned} \tag{79}$$

For the coefficient of $\partial u/\partial\xi$:

$$\left(-2\zeta-2d^2-2\frac{p^2}{e^2}\zeta\right)=-2\left[\zeta\left(1+\frac{p^2}{e^2}\right)+d^2\right]. \tag{80}$$

For the coefficient of $\partial v/\partial\kappa$:

$$-2\left[\zeta\left(1+d^2\right)+\frac{p^2}{e^2}\right]=-\frac{2}{e^2}\left(\zeta+p^2\right). \tag{81}$$

Dividing through the resulting equation by -2 gives equation (50).